1 # Three-dimensional reconstruction from experimental two-
2 # dimensional images: application to irradiated metallic fuel
3

4 R. Genoni[a,b], D. Pizzocri[a], F. Antonello[a], T. Barani[a,1], L. Luzzi[a], T. R. Pavlov[b], J.J. Giglio[b] and F. Cappia[b*]
5
6 [a]*Politecnico di Milano, Department of Energy, Nuclear Engineering Division, via La Masa 34, I-20156*
7 *Milano, Italy*
8 [b]*Idaho National Laboratory, Characterization and Advanced Post Irradiation Examination Division, P.O.*
9 *Box 1625, Idaho Falls, ID 83415, USA*
10 [1] Current address: CEA, DES/IRESNE/DEC/SESC/LSC, Cadarache center, 13108 Saint-Paul-Les-
11 Durance, France.
12
13 ** Corresponding author: fabiola.cappia@inl.gov*
14

15 ## Abstract

16 This work applies reconstruction methods based on a genetic algorithm to derive 3D material properties,
17 namely porosity and percolation fraction, in irradiated U-Pu-Zr fuel with minor actinides. We provide
18 two-dimensional experimental data regarding the radial distribution of fission gas bubbles in the fuel and
19 apply the algorithm successfully developed in a companion paper to reconstruct the fuel pore structure in
20 3D which is unknown *a priori*. The algorithm returned a set of best structures that constituted the best
21 candidate solutions representing the pore phase. From these, it was possible to extract statistics on the 3D
22 percolation fraction of the reference medium and infer a mean value, the related uncertainty, and an upper
23 and lower bound of the percolation fraction. The algorithm proved able to infer this 3D property from 2D
24 information of the metallic fuel with confidence intervals, thus establishing a path to infer 3D properties
25 directly from 2D experimental images. The knowledge of such a relationship can be used to extrapolate
26 the percolation threshold with confidence interval, which is a crucial property in defining microstructure-
27 based fission gas release models of metallic fuels.
28
29 *Keywords: FUTURIX-FTA, metallic fuel, PIE, image analysis, 3D reconstruction, genetic*
30 *algorithm*

31 # 1   Introduction

32 Visualization of microstructural changes within the fuel pellet is an important source of information
33 regarding the performance of the fuel during irradiation. Several types of microscopy can be applied, e.g.,
34 optical microscopy (OM), Scanning Electron Microscopy (SEM) or Transmission Electron Microscopy
35 (TEM). In addition to qualitative analysis assessing the overall performance of the candidate fuel,
36 extraction of salient microstructure features and quantitative description of their variation within the fuel
37 is a crucial component of post-irradiation examinations aimed at enabling robust comparison of
38 performance of different fuel designs. The porosity quantification is one of the most important quantities
39 needed experimentally to validate fuel performance code predictive models, especially concerning fission
40 gas release and gaseous swelling results [1]. For instance, physics-based models that predict the onset of
41 thermal fission gas release to the fuel rod free volume following interconnection of bubbles require
42 knowledge of bubble shape and density to determine the saturation threshold triggering the release [2,3]
43 and hence would benefit from experimental data related to the 3D bubble density and distribution to

44 validate the underlying assumptions. Bubble size distribution experimental data are used as direct input to
45 calculate local bubble pressure during temperature transients [4] and are important for simulation of fuel
46 behavior during off-normal condition [5].Application of advanced microscopy for nuclear materials and
47 specifically for nuclear fuels has significantly increased over the last ten years with tremendous
48 improvements in the understanding of nuclear material microstructure and irradiation effects [6].
49 Increased attention has been paid to the application of serial reconstruction using ion beam/scanning
50 electron microscopy (FIB-SEM) imaging to determine three-dimensional (3D) microstructure from two-
51 dimensional (2D) imaging. A recent example has studied the morphology of metal-oxide interface of
52 Zircaloy cladding at different burnup to understand the change in the rate of hydrogen uptake of the
53 claddings during in-reactor life [7]. The first application on nuclear fuels was conducted on high burnup
54 sodium fast reactor mixed oxide (MOX) [8], more recently on dispersion U-Mo fuel coated with ZrN [9],
55 and high burnup UO_2 fuel [10,11]. Alternatively, X-ray tomography has been used to obtain structural
56 information [12] as well as mechanical response [13] of TRISO particles non-destructively.

57 These techniques provide fundamental information of the fuel structure, but they present some limitations
58 in some applications to nuclear fuels, particularly for high burnup metallic fuels. X-ray tomography of
59 irradiated metallic fuels has been recently performed on irradiated metallic fuel, but the overall volume
60 investigated was small ($\sim 8 \times 10^5$ μm^3) [14], likely due to the limited penetration in high atomic number
61 and dense materials, which limits the amount of fuel that can be investigated, as well as the practical
62 limitations to bring large quantities of irradiated fuels to synchrotron facilities.

63 Metallography of metallic fuels has been extensively collected over the decades, showing pores as big as
64 hundreds of microns [15–19]. The size of those features largely exceeds the current FIB-SEM-based
65 milling and reconstruction capabilities, which are generally limited to milling areas of the order of tens of
66 microns. Hence, FIB-SEM reconstruction of pore phase in metallic fuels would not be able to capture
67 such features, which account for most of the porosity. Moreover, the number of metallography samples
68 that are prepared and analyzed in hot cells ranges between 2-3 up to tens of samples for each single rod.
69 The time and cost to manage this problem by performing serial reconstruction on each sample for all
70 possible microstructures is clearly prohibitive. Moreover, when dealing with highly radioactive nuclear
71 fuels, which imply additional handling challenges and damage to the FIB-SEM detectors, the time and
72 costs associated with the analyses increase drastically.

73 A more cost-effective approach is the reconstruction of the structure of 3D random multiphase materials,
74 such as the porous irradiated fuel, from the information obtained from a two-dimensional image. Such
75 approach, despite intrinsically ill-posed, is of great value and routinely applied in a wide variety of fields
76 (e.g., biology and petroleum engineering) when only 2D images are available for analysis [20]. There are
77 several approaches used from reconstruction of microstructures from 2D images, including simulated
78 annealing [20], Gaussian random fields [21], and genetic algorithms (GA) [22].

79 In this work, we study the fission gas bubbles of irradiated metallic fuels with a combination of image
80 analysis and an optimization technique based on a genetic algorithm [23]. We provide quantitative
81 information regarding the characteristics of the porosity in 3D in irradiated U-Pu-Zr fuel with minor
82 actinides to obtain a correlation between the 3D properties, such as the percolating fraction of the
83 porosity, and the experimentally measurable 2D quantities.

84 The paper is organized as follows. In Section 2, materials and methods, a description of the experimental
85 fuel sample and image processing to extract useful information for the reconstruction procedure is
86 introduced. Then the reconstruction procedure based on GA is briefly outlined, with particular care being
87 paid to the definition of the optimization problem and to the 3D model of the porosity adopted for

88 reconstruction. At the end of Section 2, the algorithm for the computation of the percolation fraction is
89 presented. In Section 3, results and discussion, the experimental data are first introduced and thoroughly
90 described. Then, the results of the reconstruction procedure applied to the experimental data are presented
91 and, in the end, the 3D porosity and 3D percolation fraction of each reconstructed 3D microstructures are
92 computed and discussed.

93 2   Materials and methods

94 2.1   Fuel sample and image analysis

95 The sample used in this work belongs to the FUTURIX-FTA irradiation campaign conducted in the
96 Phénix reactor as part of a joint collaboration between the U.S. Department of Energy (DOE) and the
97 French Commissariat à l'Énergie Atomique et aux Énergies Alternatives (CEA). Extensive details about
98 the irradiation campaign can be found in [24] and in the manuscripts reporting the post-irradiation
99 examinations [19,25]. The sample, which belonged to the experiment DOE1, was constituted by a
100 metallic alloy with nominal composition 34.1U-28.3Pu-3.8Am-2.1Np-31.7Zr (wt%) and predicted
101 discharge burnup of 9.1% Fission of Initial Metallic Atoms (FIMA). The post-irradiation examinations
102 showed that the presence of minor actinides did not significantly alter the overall performance of the
103 alloy, compared to historical PIE on U-Pu-Zr fuels [19]. The Zr content of the DOE1 experiment is
104 different from the "typical" Zr content of the ternary U-Pu-Zr alloys used as reference fuel in U.S. (30
105 wt.% vs. 10 wt.%) [26]. The PIE on FUTURIX-FTA DOE1 showed that the higher Zr content limited the
106 anisotropic growth and swelling of alpha-uranium, and most of the porosity remained fairly circular,
107 suggesting an underlying cubic structure [19]. A simple and isotropic pore structure compared to what
108 observed in the other alloys is advantageous for application of reconstruction methods like the one here
109 proposed, which relies upon the assumption that the pores can be modelled using randomly distributed
110 overlapping spheres.

111 Figure 1 shows a low magnification overview of the fuel cross section from Ref. [19]. Quantitative image
112 analysis was performed on images acquired with magnification 200X with a pixel spatial resolution of
113 4.81 pixels/µm using a Leica DMi8 microscope installed in the hot cell at the Hot Fuel Examination
114 Facility (HFEF) at Idaho National Laboratory (INL). The images were processed in order to obtain a final
115 binary mask of the initial microstructure representing the fuel as a two-phase material composed of the
116 solid phases (in white) and the pore phase (in black). Complete details about the image processing can be
117 found in the Appendix A. Once the image was binarized, the two-dimensional (2D) porosity, defined as
118 the fraction of area occupied by the black phase, was calculated. Simultaneously, other statistical
119 information was extracted, namely: the pore number density in 2D, the 2D pore size distribution by
120 calculating the equivalent diameter of each pore, and two statistical correlations (i.e., the two-point
121 correlation function and the lineal path function). Those two are defined after Ref. [27] and were already
122 summarized in the first part of this work [23]. 2D porosity, pore size distribution and pore density are
123 used as reference with the 2D sections of the reconstructed material, while the statistical correlations are
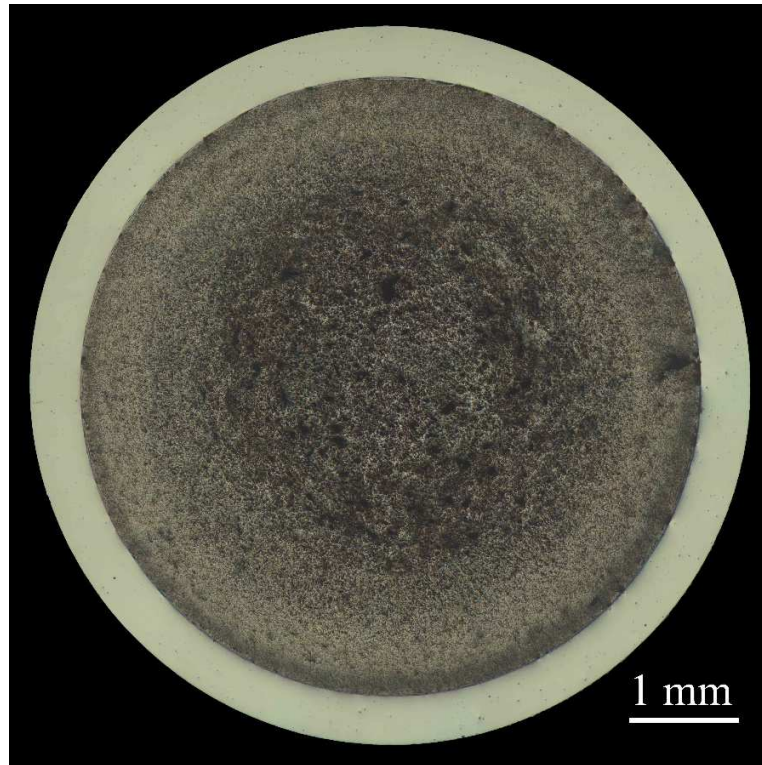124 verified *a-posteriori*.

Figure 1. Overview of the FUTURIX-FTA DOE1 sample [19].

2.2   Reconstruction methodology

The reconstruction procedure of 3D microstructures from 2D images can be treated as an optimization problem. However, the difficulties implied in the application to 3D reconstruction – such as multi-object optimization, the generally unchartered nature of the functional search space, and the inherent complexities of the 3D model of the microstructure – make this a complex optimization problem that cannot be properly faced with traditional optimization methods (e.g., the gradient method). In this work, we opted for the adoption of the reconstruction procedure based on a GA presented by the authors in a separate publication [23]. The genetic algorithm has the best features for the resolutions of complex optimization problems defined by unknown functional space [22,28]. Indeed, when there is no *a priori* knowledge of the properties of the search space, it is extremely difficult to locate a good solution that can be used as a starting point for a traditional optimization method, making the employment of heuristic methods preferable.

The development of the genetic algorithm applied to the reconstruction procedure has been already treated in detail in [23]. Here we briefly recall the main features of the reconstruction process. This reconstruction algorithm randomly samples an initial population of solutions (i.e., 3D structures of a porous material) rather than a single solution as in the traditional optimization methods. Once the 3D structures are created, one random 2D section is extracted from each 3D structure. It then ranks the solutions based on the quantitative similarities between the 2D sections from the modeled structures and the reference image of the experimental section. The information from the best ones is then used to produce a new population. The best solutions are ranked according to Pareto's efficiency, since the problem of 3D reconstruction is a multi-object optimization. It must be noted that generally with this ranking method there can be multiple solutions with the same rank, therefore the optimal solutions are

147   more than one and belong to Pareto's front. This process is repeated until the algorithm gets to a favorable
148   set of solutions that converge to the global optimum [29]. Indeed, sampling many solutions across the
149   search space improves exploration properties [30,31], increasing the likelihood that the algorithm locates
150   the global optimum and converges to it once it is located.

151   The initial model used to create the simulate 3D structures is a free parameter and needs to be established.
152   The choice of the 3D radius-distribution of the spherical pores is extremely important to the
153   reconstruction procedure and must be inquired to understand which model is the most feasible to
154   reproduce the experimental 2D pore-size distribution and correlations. This information must have
155   physical meaning. That is, it must be justified with physical arguments as well as modelling ones, as
156   discussed below in this section.

157   It is possible to infer this information by analyzing the experimental 2D images (Figure 2a) and
158   confronting them with 2D images taken from artificial 3D microstructures described by different models
159   of the pore-phase (Figure 2b). First of all, assumptions regarding the distribution of the pore phase must
160   be made. The simplest approach is to simulate the pore phase as a system of overlapping, spatially
161   randomly distributed spheres. This assumption is justified by the observation of the experimental two-
162   point correlation function (Figure 3b), which shows an exponential decay typical of a system of
163   overlapping spheres [27].

164   As for the initial 3D size distribution, the 2D images of metallic fuel generally follow a pore-size
165   distribution that resembles a lognormal, yet much more skewed, with a sharper peak and a lower shoulder
166   at the larger pores than the corresponding lognormal with the same average and standard deviation
167   (Figure 2a) [32].

168   The lognormal distribution for 3D spherical pores accounts for several physical processes that are
169   characterized by small percentage growth [33]. Thus, the lognormal distribution best describe the physical
170   processes of nucleation, growth, and coalescence of pores throughout the irradiation time in metallic fuels
171   [19]. Albeit it is effective in producing the larger pores belonging to the shoulder of the distribution, it is
172   inadequate in capturing the smaller pores belonging to the peak visible in Figure 3a. The contrary is true
173   for the single-sized distribution that can catch only the smaller pores in the peak and not the largest in the
174   shoulder, highlighting the presence of smaller pores that have nucleated too recently to have grown and
175   coalesced. The different abilities of the single-sized model to catch the peak and the lognormal model to
176   catch the shoulder suggest that the spherical pores might experimentally follow a linear combination of
177   two distributions. In fact, it should be reminded that any measured PIE data is the integral result of
178   various phenomena occurred at different stages of irradiation. The single-size distribution captures the
179   pores at the peak of the 2D pore-size distribution and the lognormal captures the behavior of larger,
180   coalesced pores at the shoulder of the 2D distribution. This result can be matched with *heuristic trials* to
181   yield the following.

182   The trials were able to produce 3D microstructures whose 2D images matched both visually (Figure 2)
183   and statistically (Figure 3) the experimental image. Model tailoring was performed on three such images.
184   Although operating on few images might present a statistical limitation, the number of pores in these were
185   such (more than 2,000) to provide enough statistical information to infer the 3D model faithfully enough.
186   The resulting distribution is a hybrid microstructure defined by lognormal distributed spherical pores and
187   single-sized spherical pores. The statistical information measured from 2D sections taken from
188   realizations of 3D structures based on the aforementioned model resemble the most the information
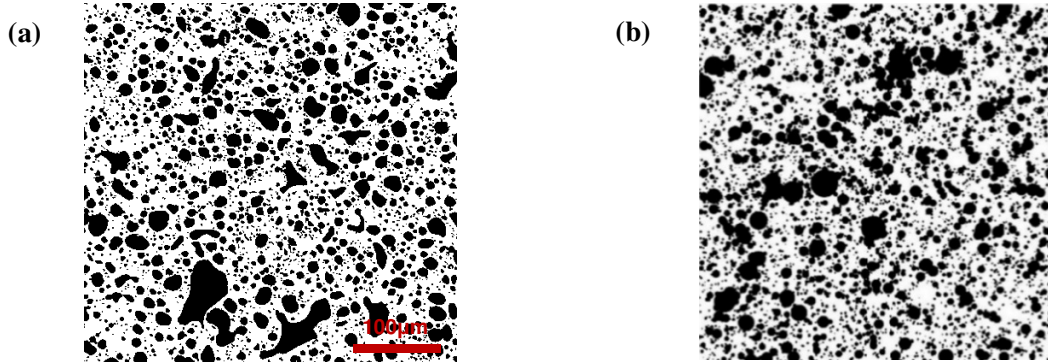189   measured from the experimental reference 2D section.

Figure 2. FUTURIX-FTA [32] 2D section (a) and reconstructed 2D section (b).
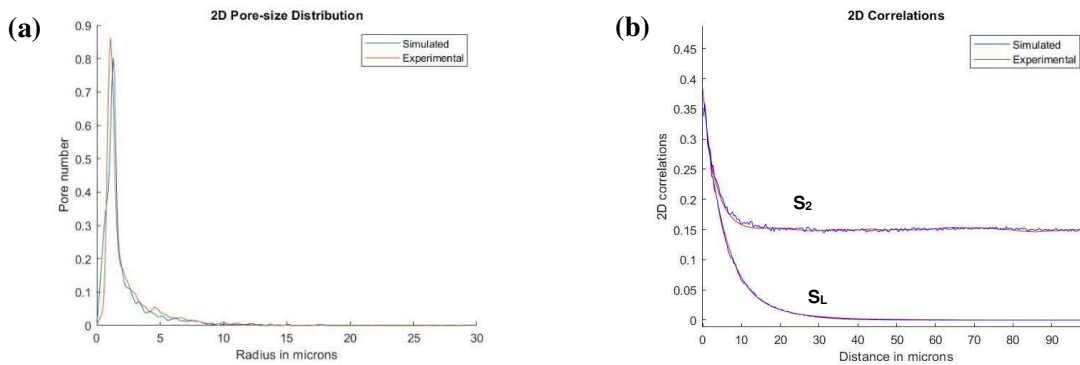
190

191

Figure 3. Comparison between the FUTURIX-FTA fuel experimental (red) and the simulated (blue) 2D pore-size distribution (a) and 2D correlations (b) yielded by a linear combination of a lognormal and a single size 3D spherical pore-size distribution.

2.3 Percolation algorithm

193 The percolation algorithm developed in this work computes the percolation fraction − i.e., the fraction of
194 volume of the 3D medium that belongs to clusters of pores that span the 3D medium from one side to the
195 opposite in either one of the three directions [34].

196 It must be stressed that an algorithm of this kind cannot be directly applied to a continuous model, hence
197 the reconstructed 3D microstructure must be digitized. Even the experimental images have an intrinsic
198 error because of digitization when passing from the physical sample to the digitized image. Digitization
199 introduces systematic errors with respect to the continuum at the pixel scale. Thus, the finer the
200 discretization, the less the deviation from the continuum [35]. The structure that can be reconstructed
201 should not have a higher resolution than the experimental reference, as having a model with higher
202 resolution than the images used to generate the system would be useless as it would exceed the length
203 scale of the problem [13].

204 Connectivity between voxels influences the percolation calculation. The limit definitions of connectivity
205 between voxels are 6 (*face to face*) and 26 (*face to face*, *corner to corner*, *edge to edge*) [35]. They
206 introduce respectively the least and the largest number of possible paths across the pore phase of the

207   medium. Therefore, they constitute the smallest and the largest overestimation of the pore phase
208   connected volume.

209   A swift study of the upper and lower bound of the percolation fraction – here as a fraction to the total
210   volume – is presented in Figure 4a and 4b adopting a single-sized and lognormal model, respectively. It
211   can be observed that different connectivity yields significant difference between the upper and lower
212   bounds at the lower porosities, but the difference significantly reduces for large values of the porosity
213   (i.e., >30%).

(a) **Single Size**   **(b)** **Lognormal**
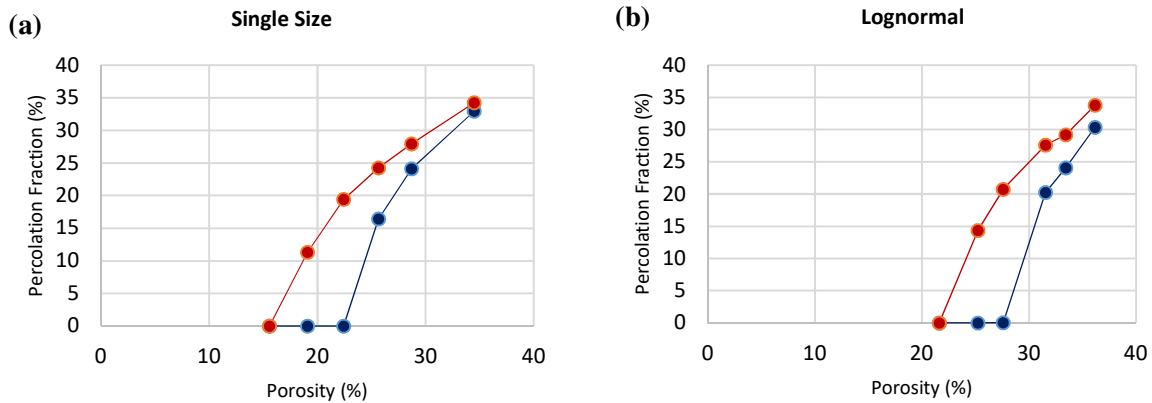
Figure 4. Percolation fraction curves for single-size pores (a), and lognormal (b), connectivity 26 (**red**) vs. connectivity 6 (**blue**).

3   Results and discussion

3.1   Experimental data

216   The porosity values measured in each image are shown in Figure 5. Together with the porosity values, the
217   local pore density (number of pores per unit area) was obtained, and is reported in Figure 6. Additional
218   statistical information is shown in Figure 7 and Figure 8, which report pore size distribution and two
219   statistical functions, respectively. In this case, the values are reported for a peripheral region of the fuel
220   and for the center. A collage of images has been performed in order to analyze a larger total area to
221   ameliorate the statistics. The total area analyzed for each region was 0.43 mm^2. In Figure 8, the statistical
222   descriptors measured are the two-point correlation function (Figure 8a), which provides information on
223   how the two end points in the pore phase are spatially correlated, and the lineal-path function (Figure 8b)
224   which is the probability that a line segment of length z lies wholly in the pore phase when randomly
225   thrown into the image. This second function captures connectedness aspects of the pore phase.
226
227   The trend of the measured porosity reported in Figure 5 is consistent with the qualitative appearance of
228   the cross section in Figure 1, in which the fuel surface appears homogeneous throughout most of the fuel
229   radius, while it is clear that the outermost part of the pellet (corresponding to $r/r_0 \approx 0.60\text{-}1$) has less
230   porosity. Although the porosity is decreasing, the number of pores increases as shown in Figure 6,
231   meaning that the average pore size is decreasing. This behavior is reflected in the pore-size distribution
232   reported in Figure 7. There is a clear decrease in the number of larger pores in the periphery, which,
233   despite less numerous, contribute most to the porosity. The different size-distribution is also reflected in
234   the statistical correlations. The faster decay of the lineal path function measured at the fuel periphery in
235   Figure 8b is a sign of the lower connectedness of the pore phase on the fuel periphery. The change in the
236   porosity trend coincides with the phase separation reported by Wright et al. [25] by Electron Probe Micro

237   Analysis (EPMA). Starting at radial position $r/r_0 = 0.6$, separation of U and Zr occurred. Although the
238   explanation of the mechanism driving this separation is beyond the scope of this work, it is interesting to
239   note the correspondence between the pore phase and the metallic phases, suggesting an influence of the
240   composition on the resulting porosity and pore density across the radius. Three images have been selected
241   across the radius and used for reconstruction of the pore phase. Results are shown and discussed in the
242   next section.
243
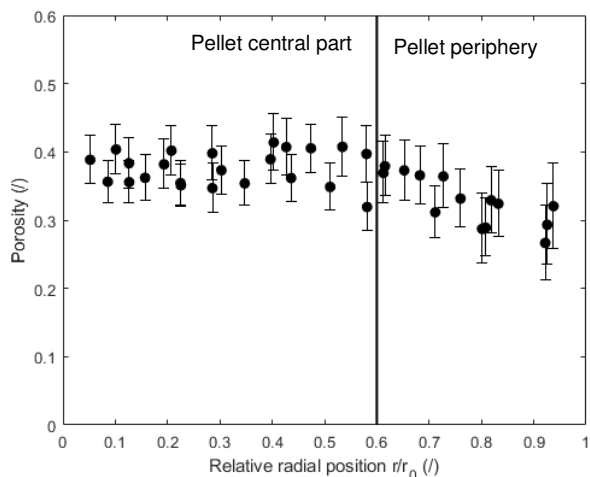
Figure 5. Porosity radial profile obtained from the image analysis. Here, the border between the central and peripheral areas of the samples can be inferred by the drop of 2D porosity, about 0.6 relative radial position from the central axis of the samples.

244
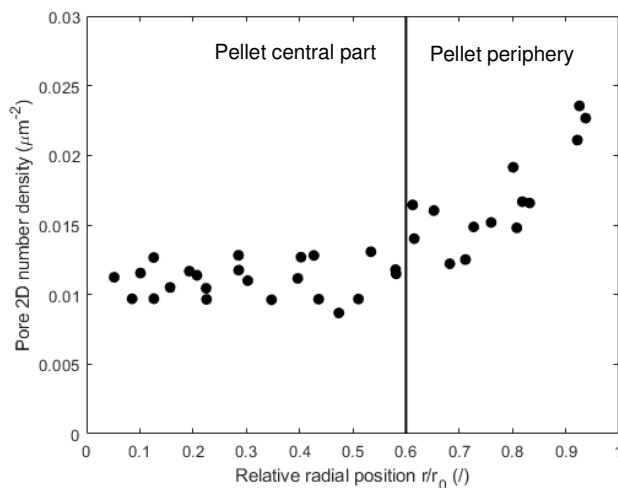
Figure 6. Radial profile of the 2D pore number density. Here the border between the central and peripheral areas of the samples can be inferred by the rise of 2D pore number density, about 0.6 relative radial position from the center axis of the samples.
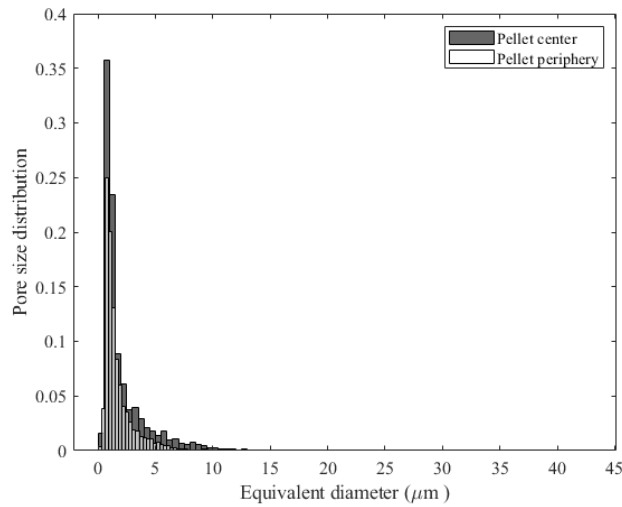
245

Figure 7. Equivalent pore diameter size distribution from the fuel center and periphery.
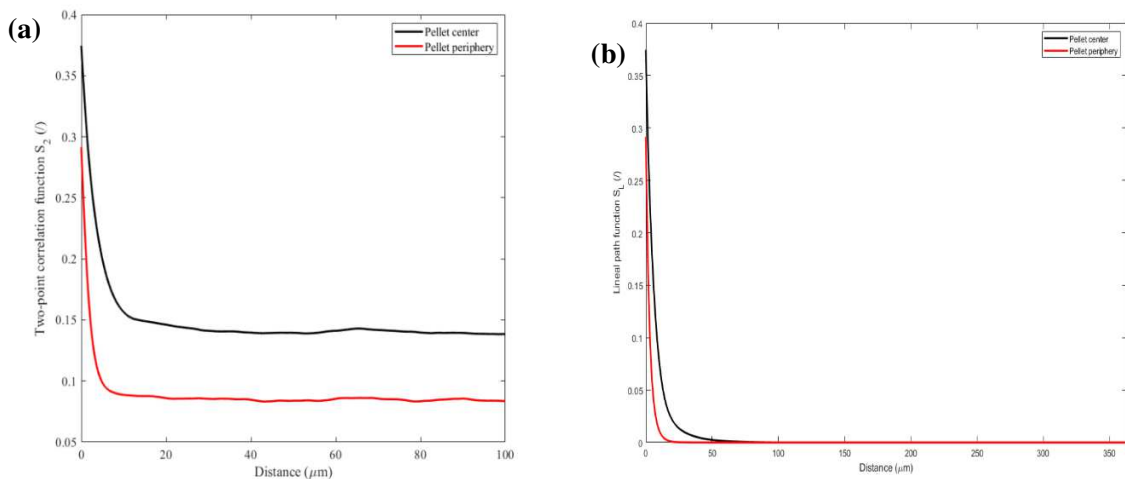
246

Figure 8. Statistical functions of the pore phase from the center and periphery of the radial cross section: (a) two-point correlation functions, (b) lineal path functions.

3.2 3D reconstruction results

248 The reconstruction procedure described in Section 2.2 is applied to three experimental images, using the
249 linear combination of a lognormal and a single-size distribution of the spherical pores previously justified.
250 The images were sampled from different radial positions across the radius of the sample.

251 The results of the 3D reconstruction are shown in Figure 9, Figure 10, and Figure 11 in terms of pore-size
252 distribution and 2D statistical correlations. The reference 2D image and one of the reconstructed 2D
253 images are also shown along. Since the 3D reconstruction procedure is based on GA applied to a multi-
254 object optimization problem, the reconstruction procedure returns a multitude of reconstructed 2D images
255 taken from as many 3D microstructures. These are the set of best solutions yielded by the 3D
256 reconstruction procedure. That is, the individuals from the last generation of the genetic algorithm that are
257 ranked as the best according to Pareto efficiency.

258 The first image (Figure 9c) was taken in the intermediate region of the cross section between 0.6 and 0.7
259 of the relative radial distance from the central axis, around the phase separation region at high U
260 concentrations [25]. In this region, there is a comparatively high density of pores (Figure 6) and a porosity
261 generally lower around 30% to 35% (Figure 5). The second image (Figure 10c) was taken between 0.2
262 and 0.3 relative radial distance and is characterized by lower pore number density (Figure 6) and higher
263 porosity (about 35% to 40%, Figure 5) than the previous image. The 3D structures are away from the
264 critical region − i.e., far from the phase transition from γ-U-Pu-Zr to the U rich one [25]. The third image
265 (Figure 11c) was taken in the central portion of the cross section − within 0.1 and 0.2 relative position,
266 with pore number density (Figure 6) and porosity similar to the second image (35% to 40%, Figure 5).

267 The comparison of the experimental and GA results is shown in Figure 9 through Figure 11. For each of
268 them, the 2D pore-size distribution, the 2D statistical correlations and the binary sections are shown. For
269 all of them, convergence is imposed on the pore-size distribution (Figure 9a, Figure 10a and Figure 11a).
270 Convergence on the pore-size distribution resulted in the convergence of the correlation functions, which
271 are also clustered around the experimental ones (Figure 9b, Figure 10b and Figure 11b).

272 The successful convergence of the GA is also qualitatively demonstrated by the comparison of the
273 experimental binary image with a 2D section cut from one of the best individuals (the optimal individuals
274 produced by the genetic algorithm), which are shown in Figure 9d, Figure 10d and Figure 11d. The
275 qualitative similarity of the reconstructed 2D images to the reference experimental 2D images highlights
276 the coherence of the model adopted in Section 2.2. The choice of overlapping spheres [34] and their
277 double 3D radius-distributions − lognormal to capture the larger, coalesced pores, and single-size to catch
278 the smaller isolated ones − could well represent the porosity structure and produce odd-shaped pore
279 features. Furthermore, the presence of many pores (more than 2,000) much smaller than the scale of the
280 image has beneficial effects for the application of the reconstruction procedure. These two features
281 provide for good statistics necessary to the reconstruction of a 3D microstructure from a single 2D
282 section.

283 There are few differences between the reference 2D images and the reconstructed ones. This is
284 nonetheless expected, since the 3D reconstruction procedure aims to reproduce 3D microstructures that
285 statistically resemble the reference one. Indeed, the 3D reconstruction procedure imposes convergence on
286 the moments of the 2D pore-size distribution (i.e., mean value and standard deviation). This feature of the
287 adopted 3D reconstruction procedure contrasts with state-of-the-art approaches, which consistently
288 impose convergence on statistical correlations [22,36,37]. However, convergence on statistical
289 correlations imposes the adoption of strong hypothesis of isotropy of the system. The adoption of
290 convergence on the 2D pore-size distribution aims at overcoming such limitations and achieve generality
291 of the 3D reconstruction procedure [23].

292 Other differences regard the shape of the pores, whose contour is smoother on the reference 2D images
293 than in the reconstructed ones. This is due to the necessary simplification of the model which treats
294 complex pore geometry as a combination of perfect spheres allowed to overlap. However, such difference
295 accounts only for exceedingly small areas and has little to no influence on the statistical properties of the
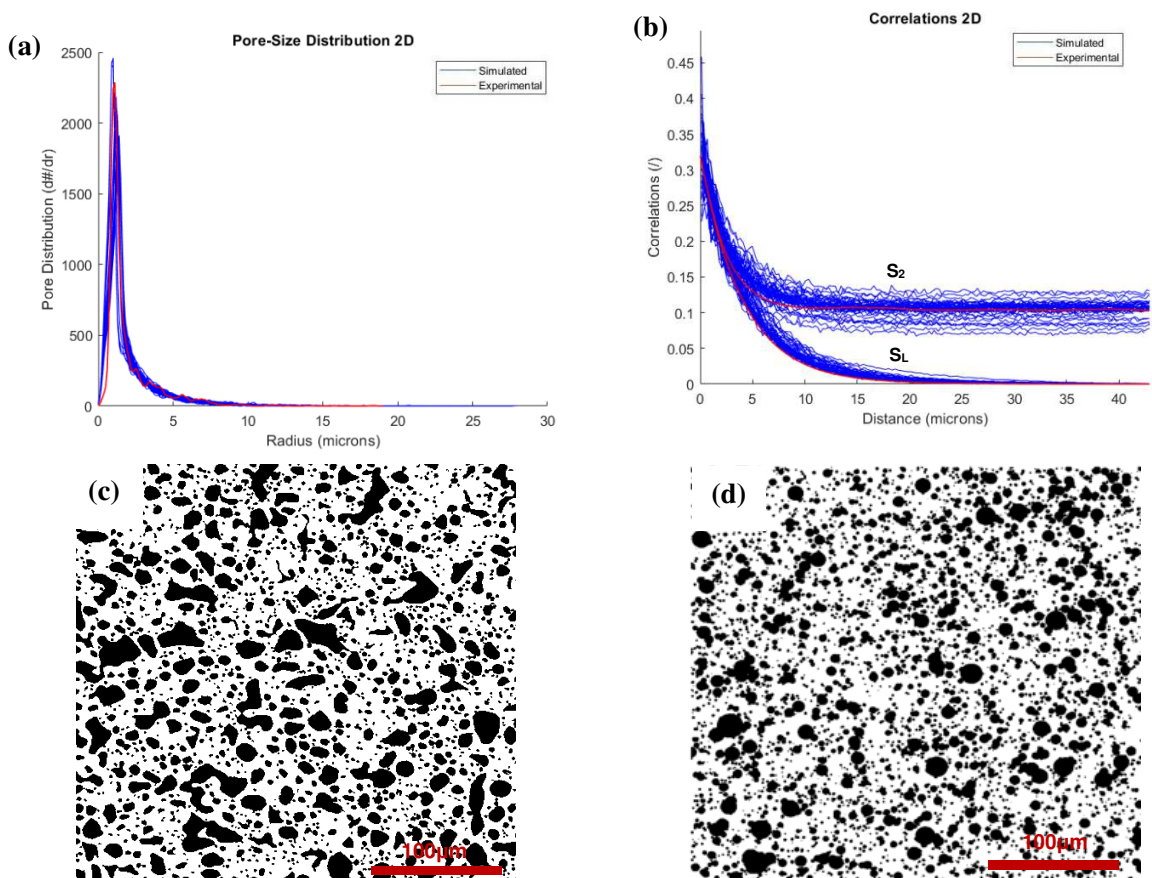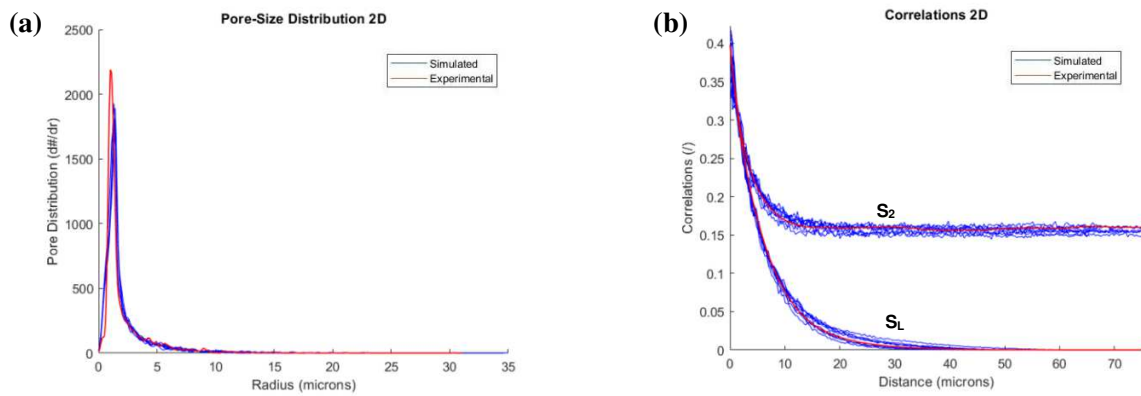296 porous medium.

Figure 9. Comparison of the GA reconstructed microstructures with the experimental data. (a) Pore size distribution, (b) Statistical correlations. In both images the experimental data is shown in red, while the GA results of the best individuals in blue. (c) Binary mask of the fuel porosity (Local porosity is 0.319). (d) 2D section obtained from one of the reconstructed microstructures.
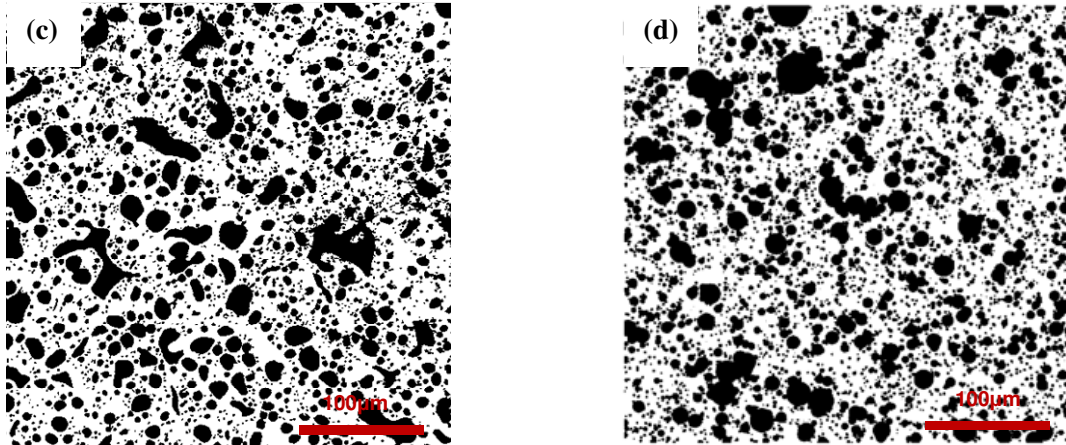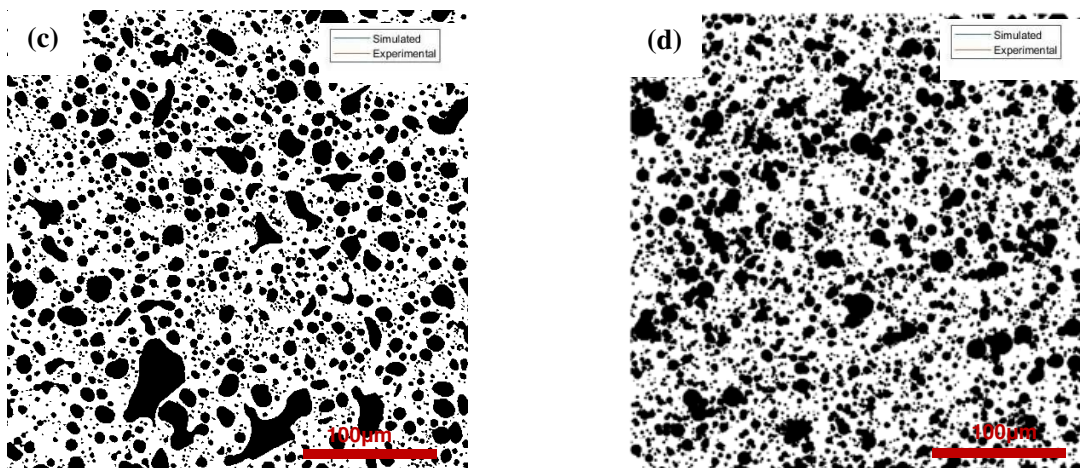
Figure 10. Comparison of the GA reconstructed microstructures with the experimental data. (a) Pore size distribution, (b) Statistical correlations. In both images the experimental data is shown in red, while the GA results of the best individuals in blue. (c) Binary mask of the fuel porosity (Local porosity is 0.397). (d) 2D section obtained from one of the reconstructed microstructures.

Figure 11. Comparison of the GA reconstructed microstructures with the experimental data. (a) Pore size distribution, (b) Statistical correlations. In both images the experimental data is shown in red, while the GA results of the best individuals in blue. (c) Binary mask of the fuel porosity (Local porosity is 0.383). (d) 2D section obtained from one of the reconstructed microstructures.

297

3.3   3D properties calculations

299 The percolation fraction is now analyzed as a function of the pore fraction of the reconstructed media. It
300 must be recalled that both terms are defined as fractions of the total volume. Since the references are at
301 high porosities (up to 30%-40% for the second and third image) the conditions are such that the difference
302 between the upper and lower bound of the percolation fraction is minimal (Figure 6). The computed
303 values are calculated using connectivity 26. The values returned are thus consistently overestimating the
304 percolation fraction of the 3D microstructure. Yet, in this field of application, the calculation of the upper
305 bound of the percolation fraction provides a conservative result from the point of view of fuel safety [16].

306   The results of the calculation of 3D percolation fraction and 2D porosity of all the 3D microstructures
307   reconstructed from each 2D image in Section 3.1 are shown in Figure 12 and summarized in Table 1. The
308   values are distributed along a curve that resembles the ones presented in Figure 3, which for higher
309   porosities converge on the bisector of the graph. Furthermore, the values of 3D porosities are in all three
310   cases clustered about the correspondent 2D porosity of the reference 2D image. These results present
311   consistency with theoretical definition of random heterogeneous material, whereas 2D porosity
312   converges to 3D porosity apart from small error at the infinite volume limit [36].

313   Being able to establish a relationship between the (measured) 2D porosity and the 3D percolation fraction,
314   the reconstruction procedure combined to the percolation fraction calculation algorithm can be used in the
315   design phase of new metallic fuel pins and in the interpretation of past experiments. This relationship
316   would allow to correlate the gaseous swelling (i.e., the local porosity) to the fission gas release which is,
317   among others, correlated to the percolated fraction. These are two key parameters for the design and
318   performance analysis of metallic fuels.

319   In general, the importance of such results is that the proposed reconstruction procedure has proven its
320   ability in the determination of empirical relationships between 3D properties and 2D information with
321   confidence intervals whereas no clear mathematical relationship exists. Figure 12 plots the results for the
322   three experimental images to which the reconstruction has been applied. A general trend of the data starts
323   being visible, suggesting that with more images at different porosities it is possible to populate the space
324   and extract the empirical law tying the 2D porosity of metallic fuel to the average 3D percolation fraction
325   with confidence intervals. By means of an empirical law available it is possible to extrapolate the value of
326   the percolation threshold of the pore microstructure of metallic fuel, which is also a quantity of interest
327   for the study of fission gas release, with the respective confidence intervals. Overall, the reconstruction
328   procedure has thus proven to be a valuable tool for the inferring of 3D properties from 2D information.
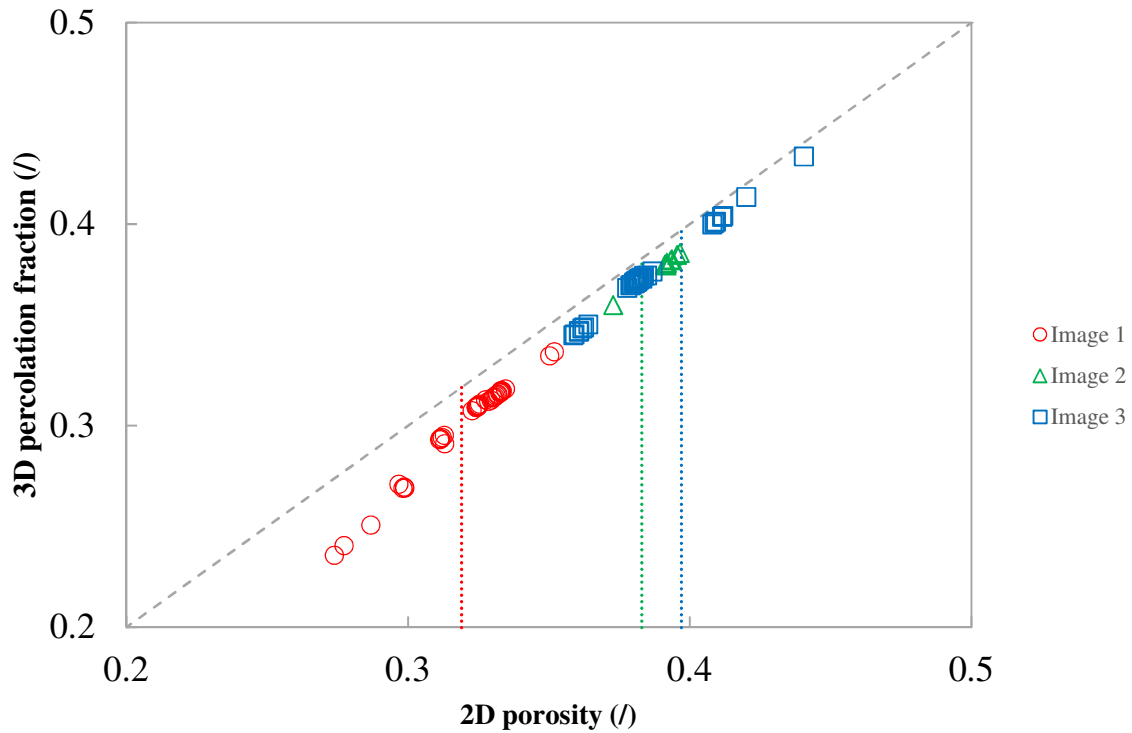
Figure 12. Properties of every 3D microstructure reconstructed compared with the 2D porosity value of the respective reference 2D image represented by the dotted lines of respective color.

329

330 **Table 1: Summary of the 3D percolation values vs. the experimental 2D porosity values.**

Image number	2D experimental porosity	3D percolation fraction	3D percolation fraction lower bound	3D percolation fraction upper bound
Image 1	0.319	0.302±0.003*	0.236	0.337
Image 2	0.383	0.379±0.002	0.360	0.386
Image 3	0.397	0.374±0.003	0.345	0.433

*The indicated error represents the standard error

331

4 Conclusions

333 The phenomenon of fission gas swelling has impact on component redistribution [38,39], thermal
334 conductivity [40], and transient behavior [41]. Therefore, it is of great importance for fuel safety
335 assessment. It is known that the swelling behavior is related to the fuel phases and textures created during
336 irradiations [39,40], but until now no investigation of the pore phase properties such as percolation
337 thresholds has been conducted.

338 This information is obtainable only directly from knowledge of the 3D structure, that is not easily
339 obtainable through direct methods (e.g., Micro-CT and FIB). Indirect methods such as reconstruction
340 procedures are favored for this kind of materials, however the complexity of the pore phase generated in

341 metallic fuel and the lack of understanding of the underlying physical phenomena driving the swelling
342 pose a serious challenge to the effectiveness of the reconstruction.

343 The algorithm successfully developed in a companion paper [23] could be applied to the reconstruction of
344 experimental media with 3D features unknown *a priori*, and the percolation fraction of these structures
345 was calculated. The procedure returned a set of best structures that constituted the best candidate solutions
346 representing the unknown microstructures. From these, it was possible to extract statistics on the 3D
347 properties of the reference medium and infer a mean value, the related uncertainty, and an upper and
348 lower bound to these properties (see Table 1). This was applied to the calculation of the percolation
349 fraction, and the algorithm proved able to infer this 3D property from 2D information of the metallic fuel
350 with confidence intervals. Further application of the reconstruction procedure to lower porosity images of
351 metallic fuel can be used to extract more useful data for the determination of a comprehensive empirical
352 relationship between 2D porosity and 3D percolation factions. The knowledge of such a relationship can
353 be useful in extrapolating the percolation threshold with confidence interval, which is a crucial property in
354 defining the irradiation performance of metallic fuel.

355 The application to the nuclear field of this procedure is only one option, and the algorithm can be applied
356 to the modelling of material phases of any solid-state material that can be modelled as a random
357 heterogeneous material.

Disclosure statement

Acknowledgements

References

371 [1] J. Rest, M.W.D. Cooper, J. Spino, J.A. Turnbull, P. Van Uffelen, C.T. Walker, Fission gas release
372   from UO2 nuclear fuel: A review, J. Nucl. Mater. 513 (2019) 310–345.
373   doi:https://doi.org/10.1016/j.jnucmat.2018.08.019.

374 [2] G. Pastore, L. Luzzi, V. Di Marcello, P. Van Uffelen, Physics-based modelling of fission gas
375   swelling and release in UO_2 applied to integral fuel rod analysis, Nucl. Eng. Des. 256 (2013) 75–
376   86. doi:https://doi.org/10.1016/j.nucengdes.2012.12.002.

377 [3] P.C. Millett, M. Tonks, S.B. Biner, Mesoscale modeling of intergranular bubble percolation in
378   nuclear fuels, J. Appl. Phys. 111 (2012) 83511. doi:10.1063/1.3702872.

379 [4] K. Kulacsy, Mechanistic model for the fragmentation of the high-burnup structure during LOCA,

380   J. Nucl. Mater. 466 (2015) 409–416. doi:https://doi.org/10.1016/j.jnucmat.2015.08.015.

381   [5]   L.O. Jernkvist, A review of analytical criteria for fission gas induced fragmentation of oxide fuel
382   in accident conditions, Prog. Nucl. Energy. 119 (2020) 103188.
383   doi:https://doi.org/10.1016/j.pnucene.2019.103188.

384   [6]   T.J. Gerczak, C.M. Parish, P.D. Edmondson, C.A. Baldwin, K.A. Terrani, Restructuring in high
385   burnup UO2 studied using modern electron microscopy, J. Nucl. Mater. 509 (2018) 245–259.
386   doi:https://doi.org/10.1016/j.jnucmat.2018.05.077.

387   [7]   A. Baris, S. Abolhassani, Y.L. Chiu, H.E. Evans, Observation of crack microstructure in oxides
388   and its correlation to oxidation and hydrogen-uptake by 3D FIB Tomography – case of Zr-ZrO2 in
389   reactor, Mater. High Temp. 35 (2018) 14–21. doi:10.1080/09603409.2017.1392412.

390   [8]   M. Teague, B. Gorman, B. Miller, J. King, EBSD and TEM characterization of high burn-up
391   mixed oxide fuel, J. Nucl. Mater. 444 (2014) 475–480.
392   doi:https://doi.org/10.1016/j.jnucmat.2013.10.037.

393   [9]   B.D. Miller, M. Abir, A. Aitkaliyeva, A. Leenaers, B.J. Hernandez, W. Van Renterghem, S. Van
394   den Berghe, A. Winston, D.D. Keiser Jr., 3D Reconstruction of M11A2 from the SELENIUM
395   Experiment, 2017.

396   [10]   J. Noirot, I. Zacharie-Aubrun, T. Blay, Focused ion beam–scanning electron microscope
397   examination of high burn-up UO2 in the center of a pellet, Nucl. Eng. Technol. 50 (2018) 259–
398   267. doi:https://doi.org/10.1016/j.net.2017.12.002.

399   [11]   C. McKinney, R. Seibert, G. Helmreich, A. Aitkaliyeva, K. Terrani, Three-dimensional bubble
400   reconstruction in high burnup UO2, J. Nucl. Mater. 532 (2020) 152053.
401   doi:https://doi.org/10.1016/j.jnucmat.2020.152053.

402   [12]   T. Lowe, R.S. Bradley, S. Yue, K. Barii, J. Gelb, N. Rohbeck, J. Turner, P.J. Withers,
403   Microstructural analysis of TRISO particles using multi-scale X-ray computed tomography, J.
404   Nucl. Mater. 461 (2015) 29–36. doi:https://doi.org/10.1016/j.jnucmat.2015.02.034.

405   [13]   D. Liu, S. Knol, J. Ell, H. Barnard, M. Davies, J.A. Vreeling, R.O. Ritchie, X-ray tomography
406   study on the crushing strength and irradiation behaviour of dedicated tristructural isotropic nuclear
407   fuel particles at 1000 °C, Mater. Des. (2019) 108382.
408   doi:https://doi.org/10.1016/j.matdes.2019.108382.

409   [14]   J. Thomas, A. Figueroa Bengoa, S.T. Nori, R. Ren, P. Kenesei, J. Almer, J. Hunter, J. Harp, M.A.
410   Okuniewski, The application of synchrotron micro-computed tomography to characterize the
411   three-dimensional microstructure in irradiated nuclear fuel, J. Nucl. Mater. 537 (2020) 152161.
412   doi:https://doi.org/10.1016/j.jnucmat.2020.152161.

413   [15]   M.K. Meyer, S.L. Hayes, W.J. Carmack, H. Tsai, The EBR-II X501 minor actinide burning
414   experiment, J. Nucl. Mater. 392 (2009) 176–183.
415   doi:https://doi.org/10.1016/j.jnucmat.2009.03.041.

416   [16]   G.L. HOFMAN, L.C. WALTERS, T.H. BAUER, Metallic Fast Reactor Fuels, Prog. Nucl. Energy.
417   31 (1997) 83–110.

418   [17]   T. Ogata, Y. Soo Kim, A.M. Yacout, 3.23 - Metal Fuel Performance Modeling and Simulation, in:
419   R.J.M.B.T.-C.N.M. Konings (Ed.), Elsevier, Oxford, 2012: pp. 713–753.
420   doi:https://doi.org/10.1016/B978-0-08-056033-5.00075-6.

421   [18]   J.M. Harp, H.J.M. Chichester, L. Capriotti, Postirradiation examination results of several metallic

422   fuel alloys and forms from low burnup AFC irradiations, J. Nucl. Mater. 509 (2018) 377–391.
423   doi:https://doi.org/10.1016/j.jnucmat.2018.07.003.

424   [19]   J.M. Harp, L. Capriotti, H.J.M. Chichester, Postirradiation Examination of FUTURIX-FTA
425   metallic alloy experiments, J. Nucl. Mater. 515 (2019) 420–433.
426   doi:https://doi.org/10.1016/j.jnucmat.2018.12.051.

427   [20]   C.L.Y. Yeong, S. Torquato, Reconstructing random media, Phys. Rev. E. 57 (1998) 495–506.
428   doi:10.1103/PhysRevE.57.495.

429   [21]   Z. JIANG, W. CHEN, C. BURKHART, Efficient 3D porous microstructure reconstruction via
430   Gaussian random field and hybrid optimization, J. Microsc. 252 (2013) 135–148.
431   doi:10.1111/jmi.12077.

432   [22]   E. Patelli, G. Schuëller, On optimization techniques to reconstruct microstructures of random
433   heterogeneous media, Comput. Mater. Sci. 45 (2009) 536–549.
434   doi:https://doi.org/10.1016/j.commatsci.2008.11.019.

435   [23]   D. Pizzocri, R. Genoni, F. Antonello, T. Barani, F. Cappia, 3D reconstruction of two-phase
436   random heterogeneous material from 2D sections: An approach via genetic algorithms, J. Nucl.
437   Eng. Technol. in review (n.d.).

438   [24]   E. Brunon, L. Donnet, D. N, P. Jaecki, S. Pillon, F. Sudreau, D. Warin, S. Hayes, J.R. Kennedy,
439   M. Meyer, S. Willson, A. Fernandez, D. Haas, Y. Arai, The Futurix-FTA experiment in Phenix,
440   in: Actinides Fission Prod. Partitioning Transmutat., Las Vegas, 2005.

441   [25]   K.E. Wright, J.M. Harp, L. Capriotti, Electron probe microanalysis of irradiated FUTURIX-FTA
442   U-Pu-Zr alloy with added minor actinides, J. Nucl. Mater. 526 (2019) 151745.
443   doi:https://doi.org/10.1016/j.jnucmat.2019.151745.

444   [26]   D.C. Crawford, D.L. Porter, S.L. Hayes, Fuels for sodium-cooled fast reactors: US perspective, J.
445   Nucl. Mater. 371 (2007) 202–231. doi:https://doi.org/10.1016/j.jnucmat.2007.05.010.

446   [27]   S. Torquato, Microstructural descriptors, in: Random Heterog. Mater. Microstruct. Macrosc. Prop.,
447   Springer-Verlag Berlin Heidelberg & Material Phases Data System (MPDS), Switzerland &
448   National Institute for Materials Science (NIMS), Japan, 2002: pp. 23–58.

449   [28]   J. Pearl, Heuristics: Intelligent search strategies for computer problem solving., 1984.

450   [29]   H. Booker, LB; Goldberg, DE; JH, Classifier systems and genetic algorithms, Artif. Intell. 40
451   (1989) 235–282. doi:10.1016/0004-3702(89)90050-7.

452   [30]   A.B. Tarek A. El-Mihoub, Adrian A. Hopgood, Lars Nolle, Hybrid Genetic Algorithms: A
453   Review, 13 (2006) 124–137.

454   [31]   Y.A. Zhang, M. Sakamoto, H. Furutani, Effects of population size and mutation rate on results of
455   genetic algorithm, Proc. - 4th Int. Conf. Nat. Comput. ICNC 2008. 1 (2008) 70–75.
456   doi:10.1109/ICNC.2008.345.

457   [32]   F. Cappia, Post-irradiation examinations of metallic fuels: applied comusper vision methods for
458   fission gas bubbles analysis - A test case on the FUTURIX-FTA DOE1 fuel, Idaho Falls, ID, n.d.

459   [33]   E. Limpert, W.A. Stahel, M. Abbt, Log-normal Distributions across the Sciences: Keys and Clues,
460   Bioscience. 51 (2006) 341. doi:10.1641/0006-3568(2001)051[0341:lndats]2.0.co;2.

461   [34]   M.D. Rintoul, S. Torquato, Precise determination of the critical threshold and exponents in a three-
462   dimensional continuum percolation model, J. Phys. A. Math. Gen. 30 (1997). doi:10.1088/0305-

463   4470/30/16/005.

464   [35]   E.J. Garboczi, D.P. Bentz, The effect of statistical fluctuation, finite size error, and digital
465   resolution on the phase percolation and transport properties of the NIST cement hydration model,
466   Cem. Concr. Res. 31 (2001) 1501–1514. doi:10.1016/S0008-8846(01)00593-2.

467   [36]   S. Torquato, Random Heterogeneous Materials, Springer New York, New York, NY, 2002.
468   doi:10.1007/978-1-4757-6355-3.

469   [37]   C.L.Y. Yeong, S. Torquato, Reconstructing random media. II. Three-dimensional media from two-
470   dimensional cuts, Phys. Rev. E - Stat. Physics, Plasmas, Fluids, Relat. Interdiscip. Top. 58 (1998)
471   224–233. doi:10.1103/PhysRevE.58.224.

472   [38]   W.J. Carmack, D.L. Porter, Y.I. Chang, S.L. Hayes, M.K. Meyer, D.E. Burkes, C.B. Lee, T.
473   Mizuno, F. Delage, J. Somers, Metallic fuels for advanced reactors, J. Nucl. Mater. (2009).
474   doi:10.1016/j.jnucmat.2009.03.007.

475   [39]   D.L. Porter, H.J.M. Chichester, P.G. Medvedev, S.L. Hayes, M.C. Teague, Performance of low
476   smeared density sodium-cooled fast reactor metal fuel, J. Nucl. Mater. 465 (2015) 464–470.
477   doi:10.1016/j.jnucmat.2015.06.014.

478   [40]   T. Ogata, Metal fuel, 1st ed., Elsevier Inc., 2012. doi:10.1016/B978-0-08-056033-5.00049-5.

479   [41]   G.R. Fenske, J.E. Emerson, F.E. Savoie, E.W. Johanson, Fission Gas Retention and Axial
480   Expansion of Irradiated Metallic Fuel, Argonne, Illinois, 1986.

481

Appendix A

The image processing started with pre-processing to enhance image contrast. After grayscale conversion, the contrast was enhanced by adopting the Matlab® built-in function for contrast-limited adaptive histogram equalization. The optical microscopy images showed good contrast between the large pores and the fuel matrix phase, but the simultaneous very small and shallow pores exhibited much less contrast due to their shallow nature, hence a simple binarization approach could not be implemented. The successful segmentation of the smaller pores is important to promote data accuracy as smaller pores, despite bringing little contribution to the total porosity, are relevant for pore-size distribution measurements and statistical analysis of pore spatial distribution and connectivity. Hence, we adopted a 3 steps approach, step 1 dedicated to the segmentation of the large pores and the other two to the segmentation of the small pores.

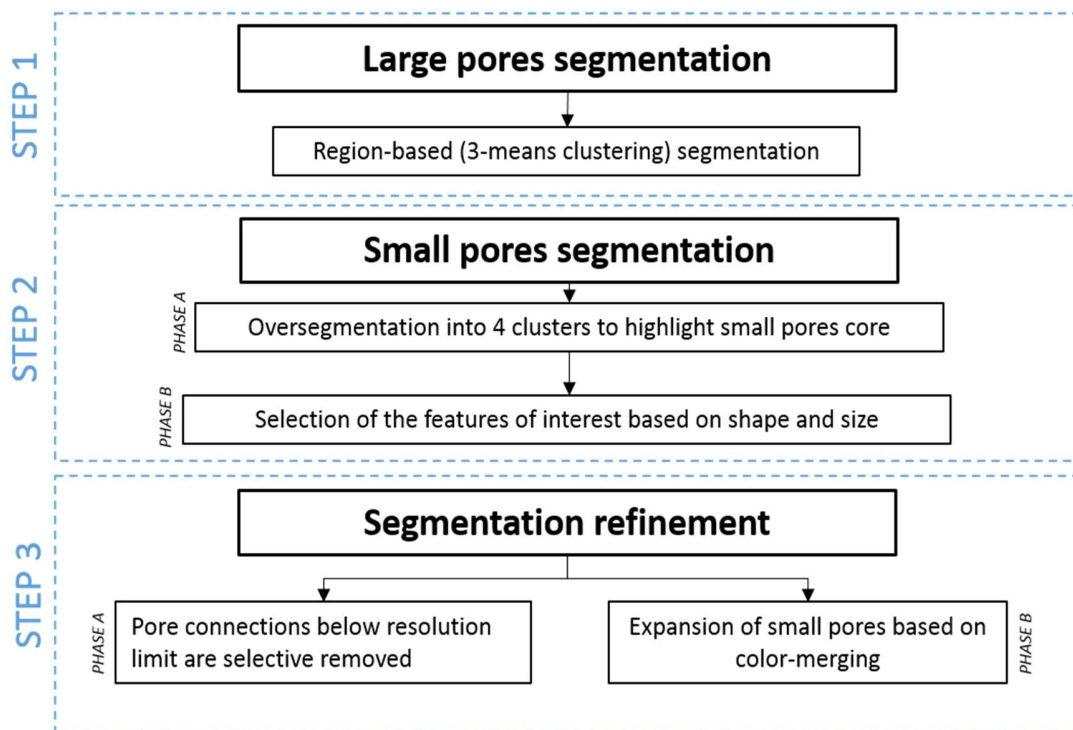A schematic overview of the algorithm is depicted in Fig. A1.

Figure A1: Algorithm scheme for the optical microscopy images.

In step 1, the good contrast allows for segmentation based on grayscale, by dividing the histogram in three clusters associated with matrix, porosity, and additional phase that encompass solid fission products precipitates. Step 2 is dedicated to the segmentation of small pores. Those are first identified by over-segmenting the image by adding an additional cluster in the region-based segmentation, as shown in Fig. A2 (see the arrows). However, since the shading of the larger pores is also identified in this procedure, an additional condition is imposed to identify only the correct features. The objects, in addition to belonging to the added gray level cluster, must have limited elongation, i.e., the major axis length must be less than three times the minor axis length. In addition, objects must be solid, i.e., the Euler number associated with the object must be one. This last condition assures that shading areas are always removed.
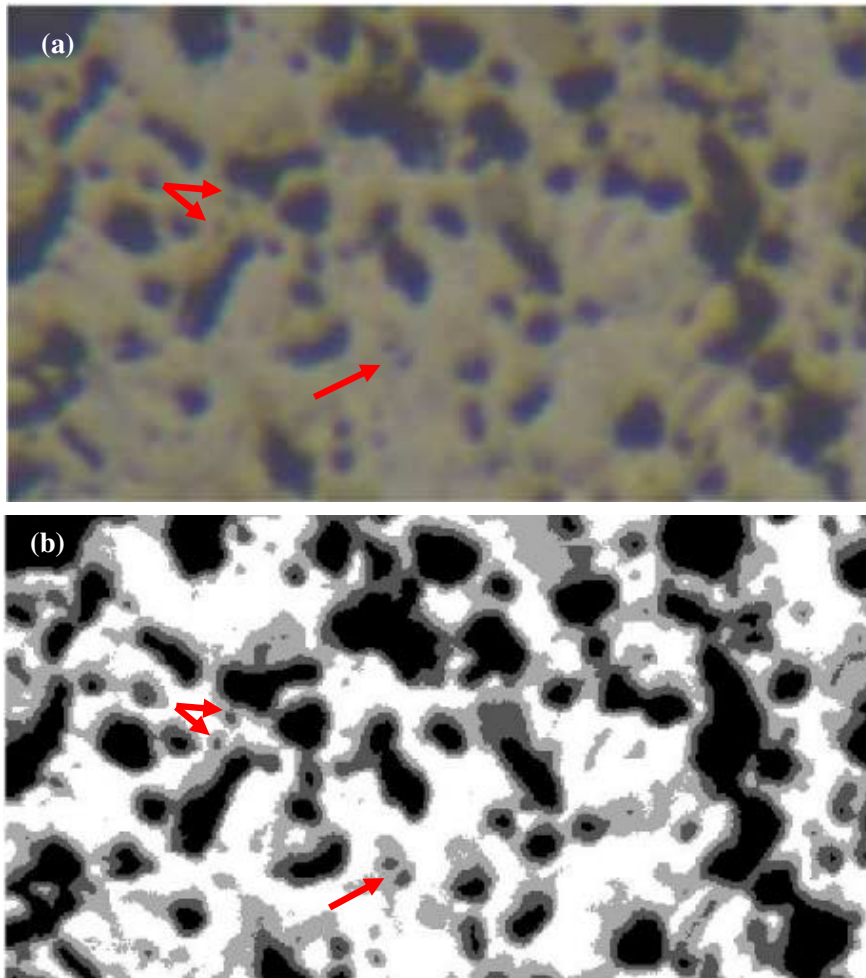
Figure A2: (a) Original image, (b) 4-means clustering used in STEP 2 to isolate the core of small pores. The red arrows highlight the small pores identified thanks to the oversegmentation.

503

504 In the last part of the algorithm, the results obtained in the previous steps are refined. Due to resolution
505 limits, some of the pores might be loosely connected in the resulting segmented image (see arrows in Fig.
506 A3a). The borders of each object are explored and if connecting lines whose thickness is equal or less
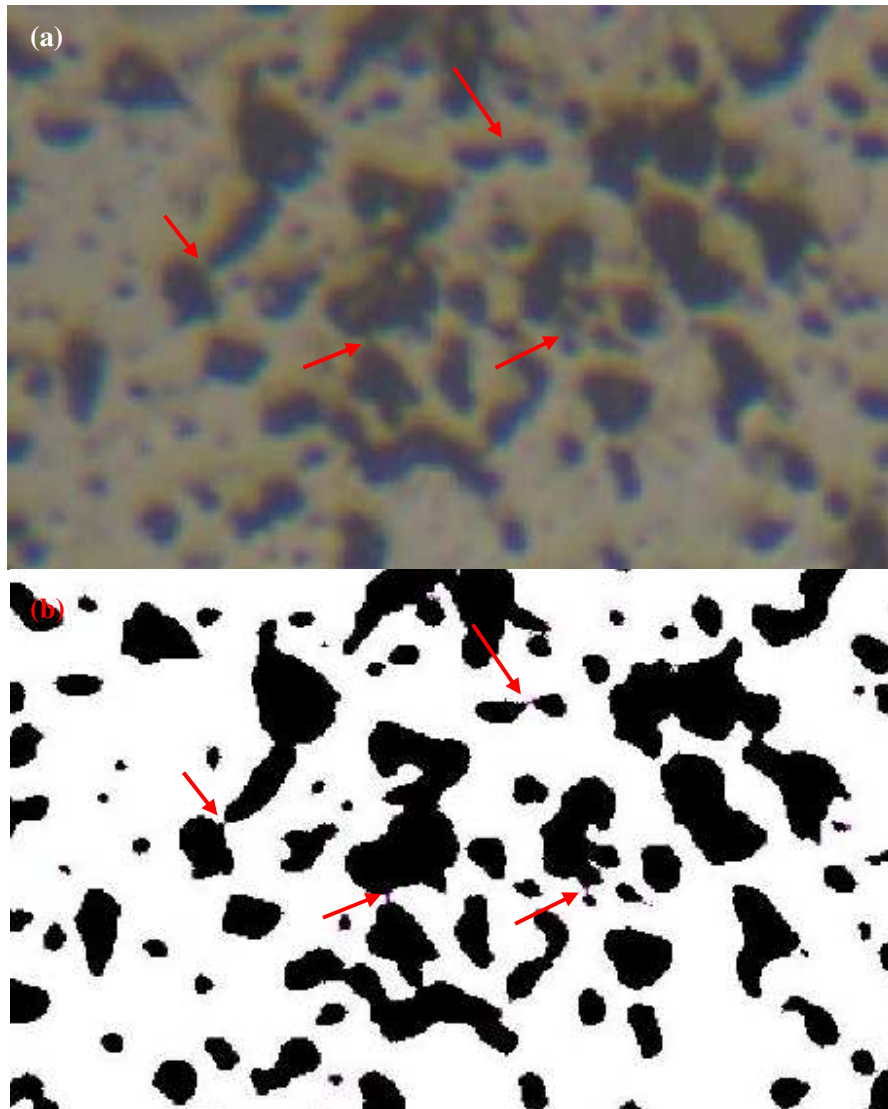507 than 2 pixels are found, they are removed (shown in pink in Fig. A3b).

Figure A3: (a) Original image. The arrows highlight pores interconnections which are due to resolution limits (b) Binary image of (a) showing the removed connecting lines indicated by the arrows.

508

509 The oversegmentation used in step 2 to identify the small pores is effective to locate the pore cores, but it
510 might lead to an underestimation of their size. Therefore, an additional sub-step is added to allow the
511 expansion of small pores (with size below 50 pixels) based on gray-level difference with the surrounding.
512 For each small pore, the average gray-value of the pore core is determined and a gray-level distance map
513 from this mean value is computed. An area of radius 10 pixels is explored around each object. If the gray-
514 value of the pixels in the examined surrounding area is within a tolerance threshold T of the average gray-
515 value of the pore core, the neighboring pixels are added to the object. The effect of variations in the
516 tolerance value on the resulting porosity measurements are evaluated and discussed in the results section.
517 Figure A4b shows the expansion of the pores when T is set to 10%.

518 Once the segmentation process is complete and the binary image obtained combining the objects
519 identified in the various steps, the statistical parameters are calculated. As the tolerance assigned during

520   the expansion is arbitrary and can impact the porosity value calculated from the image, the calculation of
521   the porosity was performed also for an expansion threshold of 5%. The results in Fig. A5 show the
522   limited impact of this parameter in the experimental porosity value, particularly when compared to the
523   uncertainty associated with overall porosity uncertainty. In fact, the sample surface curvature around the
524   pores can create uncertainties in the definition of the pore boundaries. In order to provide a conservative
525   estimation of the porosity error, both a contraction and an expansion of the pores around the pixel
526   boundaries has been performed, which gives an upper and lower value of porosity for each image showed
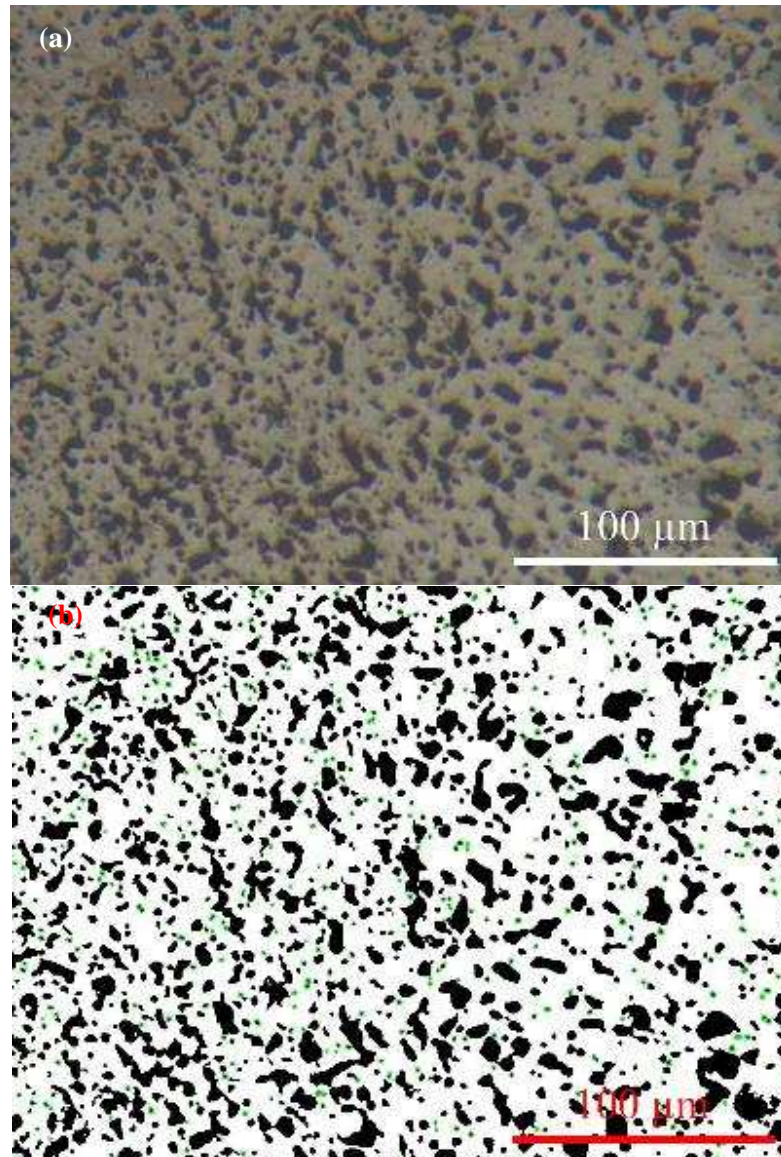527   by the error bars in Fig. A5.

Figure A4: (a) Original image. (b) Binary image of (a) showing the expanded small pores in green.
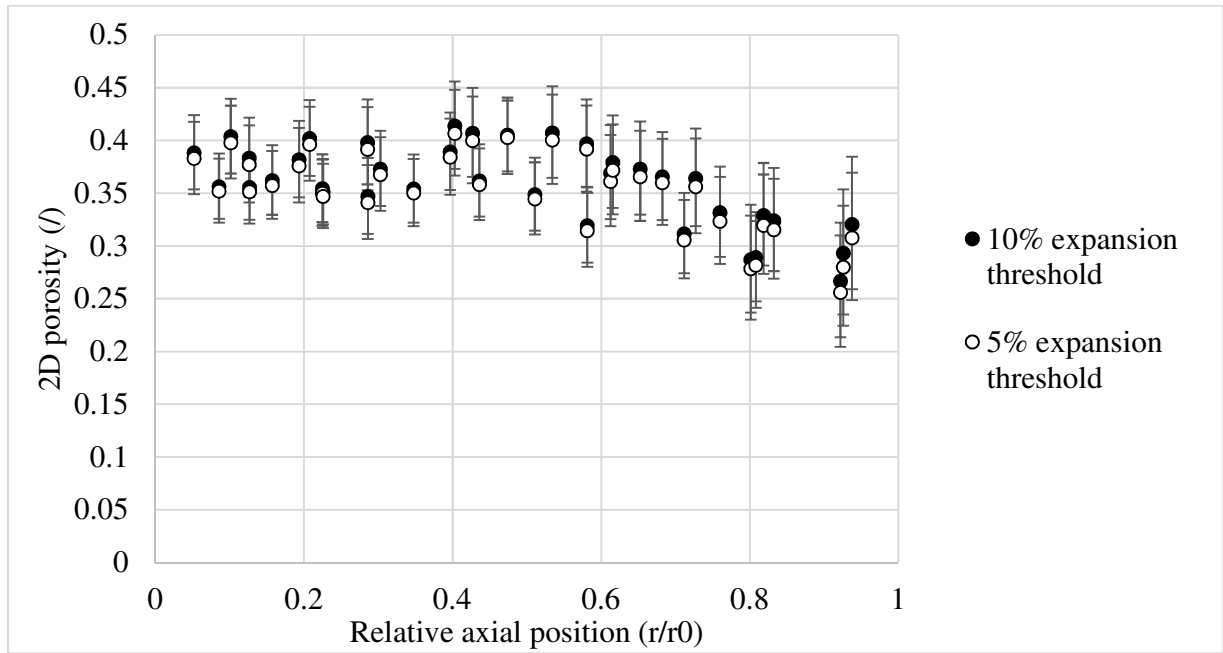
528

529

530

Figure A5: Impact on the measured porosity of the variation of the expansion threshold of small pores.

531